PAPER • OPEN ACCESS

Comprehensive model and performance optimization of phase-only spatial light modulators

To cite this article: A A Pushkina *et al* 2020 *Meas. Sci. Technol.* **31** 125202

View the article online for updates and enhancements.

You may also like

Comprehensive model and performance optimization of phase-only spatial light modulators

A A Pushkina[1] , **J I Costa-Filho**[1]**, G Maltese**[1] **and A I Lvovsky**[1,2,3]

[1] Department of Physics, University of Oxford, Oxford OX1 3PU, United Kingdom
[2] Russian Quantum Center, 100 Novaya St., Skolkovo, Moscow, 143025, Russian Federation
[3] P. N. Lebedev Physics Institute, Leninskiy prospect 53, Moscow, 119991, Russian Federation

E-mail: alex.lvovsky@physics.ox.ac.uk

CrossMark

Abstract
Several spurious effects are known to degrade the performance of phase-only spatial light modulators. We introduce a comprehensive model that takes into account the major ones: curvature of the back panel, pixel crosstalk and the internal Fabry–Perot cavity. To estimate the model parameters with high accuracy, we generate blazed grating patterns and acquire the intensity response curves of the first and second diffraction orders. The quantitative model is used to generate compensating holograms, which can produce optical modes with high fidelity.

Keywords: spatial light modulator, pixel crosstalk, back panel curvature, internal Fabry–Perot cavity, spurious effects compensation, compensating holograms

(Some figures may appear in colour only in the online journal)

1. Introduction

The ability to tailor structured light beams with arbitrary intensity and phase spatial profiles is a cornerstone for a vast range of active fields, such as quantum information and communication [1, 2], biomedical imaging [3, 4], optical tweezing [5, 6], holography [7], topological photonics [8], and metrology [9]. In the last decades, liquid crystal on silicon spatial light modulators (LCoS SLMs) have been established as the primary tool to generate spatially structured light beams. A LCoS SLM reshapes the wavefront of an incoming beam by controlling the effective refractive index of a liquid crystal layer pixel by pixel [10–12]. Among the various types of LCoS SLMs, reflective phase-only nematic SLMs are particularly popular [13, 14]. By making use of high-yield

CMOS backplanes (pixel pitch $\sim 10\,\mu m$, fill factor up to 98%), high diffraction efficiencies can be achieved, while the large electro-optic coefficients of liquid crystal materials enable significant modulation depths (up to several wavelengths) and real-time operation (millisecond response time) [15].

An ideal phase-only SLM should produce a predictable, linear and uniform phase response to the computer generated control voltage matrix. However, a few imperfections are known to deteriorate the SLM performance. The three most important ones are: the curvature of the back panel [16], a low-finesse internal Fabry–Perot cavity formed by the cover glass-air interface and the curved back panel [17] and pixel crosstalk [18, 19]. If not compensated, these spurious effects introduce undesirable changes to the beam wavefront.

In previous works, pixel crosstalk [20, 21], the backpanel curvature [16, 17, 22, 23] and the cavity [24] have been studied as individual phenomena, but their joint influence on the diffracted beam has not been investigated. Yet, since these effects act simultaneously, neglecting one of them leads to imprecise estimation of the others, hindering their correct compensation. In this work we propose a comprehensive model for all these effects, as well as a simple characterization procedure and

an effective compensation method. Our characterization technique relies on exploiting the interference occurring within the SLM's inner cavity and hence avoids the need for an external interferometer [17, 23], which would require careful alignment. Its further advantage is that the measurement results are specific to the SLM and not significantly affected by the external optics or its alignment.

Our method consists in generating blazed grating holograms of varying amplitude and measuring the position-dependent near-field intensity of the diffracted light in the first and second orders as a function of the grating amplitude. The second order is crucial for the accurate prediction of the model parameters, since it is more sensitive to pixel crosstalk and inner cavity effects than the first order.

The detailed knowledge of the detrimental effects permits us to compensate for them. We demonstrate this capability by preparing Hermite-Gaussian (HG) modes of high order and evaluate the preparation fidelity by measuring their profiles both in the near and far fields. In this sense, our characterization technique is more comprehensive than some of the previous methods, which rely on measuring and optimising the intensity profiles in the Fourier plane only [22, 25, 26]. Our compensation procedure stacks up to the well-known blazed grating patterns encoding method [13, 27], refining it to correct for both the backpanel curvature and the cavity effect.

As an example, we demonstrate $HG_{12,12}$ with a fidelity of 94.5%, which is 1.9% higher than the one obtained by applying a curvature only compensating hologram and 5.2% higher than the one generated by a non-corrected hologram. Furthermore, we demonstrate crosstalk correction which increases the first order diffraction efficiency by 28%.

2. Imperfections of a phase-only SLM

Figure 1 schematizes the layered structure of a phase-only reflective SLM [28]. Due to a refractive index step at the air-glass interface, an anti-reflection coating is usually applied to the coverglass surface. The resulting coverglass reflection coefficient is low (usually around 0.1 or less [24]) but not negligible. This interface and the reflective layer of the back panel form a low-finesse Fabry–Perot cavity, which produces spurious reflection from the SLM surface. In the following, we refer to this as the *cavity effect*. We note that additional reflections may occur at the interface between the coverglass and the liquid crystal, but we found them to be negligible.

The lower part of figure 1 illustrates the curved SLM backpanel leading to a non-uniform thickness of the liquid crystal layer. Each wavefront propagating in the liquid crystal layer experiences a phase retardation given by two contributions. The first one depends on the liquid crystal molecules' orientation, determined by the pixel voltage matrix (i.e. the printed hologram). The second contribution, voltage-independent, is determined by the additional optical path associated with the non-uniform liquid crystal thickness.
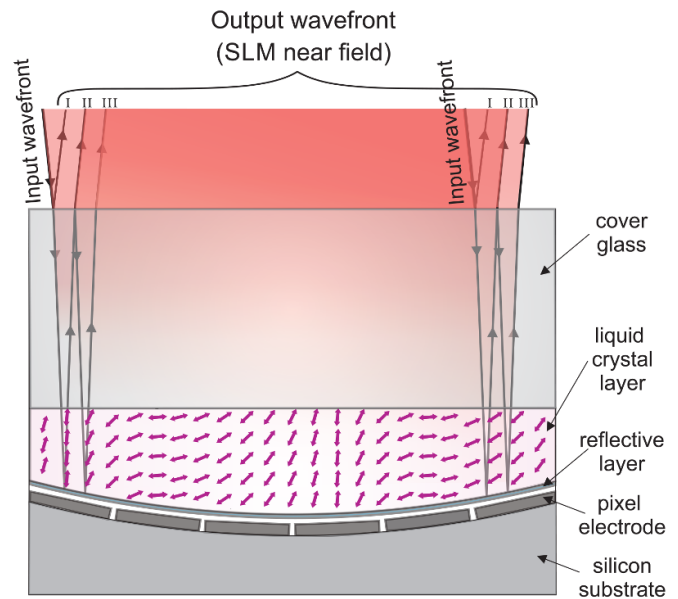

Figure 1. Schematic cross-section of a phase-only SLM illuminated by a wide laser beam. I, II, III outline the wavefronts produced by the Fabry–Perot cavity formed by the air-glass interface and the backpanel.

The final imperfection to be addressed is the crosstalk. Figure 1 shows how it alters the orientation of the liquid crystal molecules (magenta arrows) when a 3-pixel period blazed grating is printed on the SLM. At each pixel, the liquid crystal molecules are not identically oriented, but slightly aligned with the molecules in the adjacent pixels, thereby smoothing the phase profile experienced by an incoming wavefront.

3. Experiment

Figure 2 illustrates the optical setup used to characterize the SLM. We illuminate the whole screen of a reflective phase-only LCoS-SLM (Hamamatsu X13 138-02) using a continuous laser beam at 785 nm. The angle between the incoming and reflected beams is less than 5°. The polarization of the incoming beam is linear and aligned with the liquid crystal extraordinary axis. The SLM resolution is 1272×1024 pixels and the pixel pitch is 12.5 µm. At each pixel, the SLM is calibrated by the manufacturer to have a linear phase response to the control voltage, defined by an 8-bit integer number, commonly referred to as the *gray level*. The gray level inducing a 2π phase shift is called the 2π voltage. No other manufacturer-issued correction information is used aside from assuming that the phase-to-gray-level response of the liquid crystal layer is linear.

To characterize the spurious effects, we print on the SLM screen a blazed grating hologram of a 20-pixel period, varying its amplitude from 0 to 248 gray levels in steps of 2. The reflected beam is focused by a 2-inch aperture lens ($f = 250\,\text{mm}$) and subsequently re-imaged by another lens onto a CCD camera (UI-2140SE). An iris diaphragm in the focal plane of the first lens selects either the first or the second diffraction order.
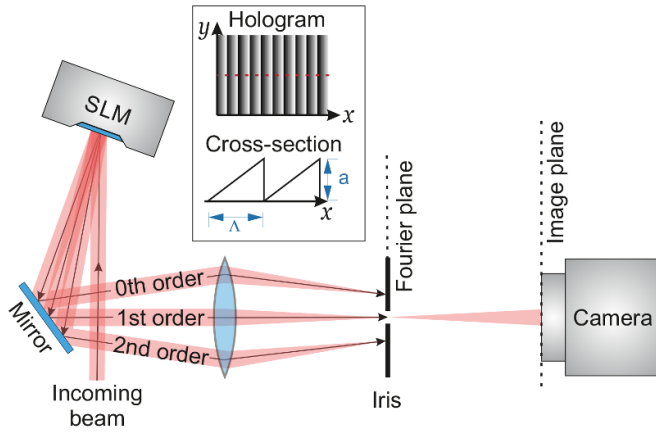
Figure 2. Experimental setup. The SLM hologram containing a horizontal blazed grating diffracts the incoming beam. An iris in the Fourier plane selects either the first or second diffraction order and a camera in the image plane acquires the intensity profile corresponding to the near-field of the SLM.
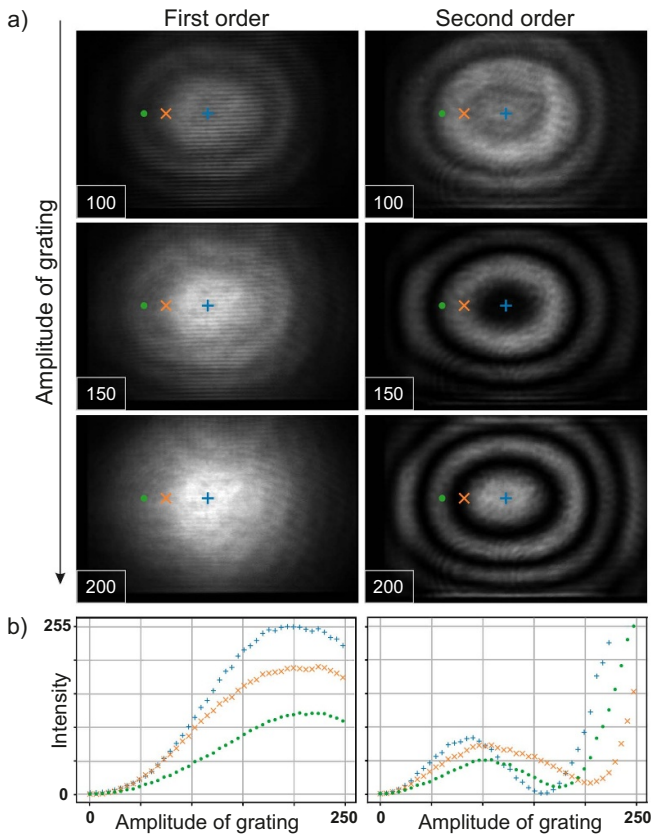

Figure 3. (a) Near-field images of the first and second diffraction orders for three different values $a = 100, 150, 200$ of grating amplitude. (b) Diffracted intensity versus grating amplitude for the three SLM sections marked in figure 3(a).

Figure 3(a) shows the near-field intensity images for three different values of grating amplitude. We notice an annular structure in the intensity profiles, which is necessarily a sign of the previously mentioned Fabry–Perot cavity effect. Specifically, it is a result of interference of the fields reflected from the

SLM after different number of passes through the liquid crystal layer of spatially varying thickness, marked as I, II, and III in figure 1. For high grating amplitudes, this structure is much more pronounced in the second order than in the first one.

Intuitively this can be understood as follows. Field I is always emitted into the zeroth order. Because of the low reflectivity of the air-glass interface, beam II is generally much stronger than beam III. But when the grating voltage is 2π, the effect of the grating upon the single-pass beam (II) becomes equivalent to that of a plane mirror directing the entire optical field towards the first order. By the same token, the double-pass beam (III) experiences a grating of amplitude 4π, so all of its energy goes into the second order. As a result, in the neighborhood of that voltage the amplitudes of wavefronts II and III in the second order become comparable with their relative phase dependent on the liquid crystal layer thickness.

This effect is further visible in figure 3(b), where we plot the integrated intensity response for the three 20×20 sections of the SLM screen centered as marked in figure 3(a). The second order intensity is low, with the behavior strongly dependent on the cavity thickness, for the grating amplitudes around the 2π voltage (~ 200 gray levels), resulting in well-defined rings.

4. Theoretical model

As illustrated in figure 1, the optical field emitted by the SLM is given by the sum over the multiple wavefronts reflected from the cavity:

$$E(x,y) = -r - t^2 e^{i\varphi(x,y)} \sum_{l=0}^{\infty} \left[-r e^{i\varphi(x,y)} \right]^l$$
$$= -\frac{r + e^{i\varphi(x,y)}}{1 + r e^{i\varphi(x,y)}}, \tag{1}$$

where r and t are the reflection and transmission coefficients of the air-glass interface, $\varphi(x,y)$ the phase accumulated by the field in each round-trip and l the number of reflections from the back panel. We assume the reflectivity of the back panel to equal 1. The phase $\varphi(x,y)$ is given by

$$\varphi(x,y) = \theta(x,y) * g(x,y) + \alpha(x,y). \tag{2}$$

The first term is due to the liquid crystal's response to the applied voltage, with $\theta(x,y)$ being the phase shift in the absence of crosstalk. The crosstalk is modelled by convolving $\theta(x,y)$ with a normalized Gaussian point spread function: $g(x,y) = \mathcal{N}\left(e^{\frac{-(x^2+y^2)}{2w^2}} \right)$. The width w ranges from a fraction of one pixel to several pixels, depending on the SLM model [20, 29], and quantifies the strength of the effect. The second, voltage independent, term, $\alpha(x,y)$, is associated with the spatially variable thickness of the Fabry–Perot cavity.

The field distribution (1) depends upon the following set of parameters: $\{r, w, a_{2\pi}(x,y), \alpha(x,y)\}$. We assume that r and w are spatially independent, while $\alpha(x,y)$ and the 2π voltage $a_{2\pi}(x,y)$ are functions of transverse position. The voltage applied to the SLM corresponds to a blazed grating with its
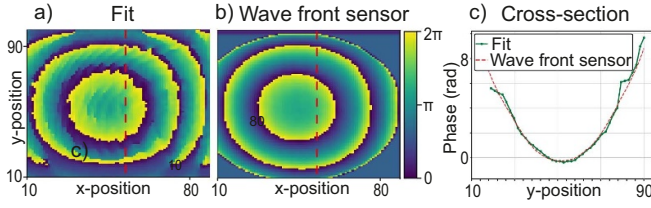
Figure 4. Phase map $\alpha(x,y)$ (a) calculated from our model fit and (b) measured with a wavefront camera. The profiles of the cross-sections marked by dashed red lines are shown in (c).

lines along the y axis:

$$\theta(x,y) = \frac{a}{a_{2\pi}} \cdot \mathrm{mod}\left(\frac{2\pi x}{\Lambda}, 2\pi\right), \qquad (3)$$

where a and Λ are the grating amplitude and period, respectively. We numerically calculate the Fourier transform of equation (1) and obtain the theoretical response curve of the first (second) diffraction order $I^{\mathrm{th}}_{\mathrm{1st(2nd)}}(a,x,y,\{r,w,a_{2\pi},\alpha\})$, which is a function of the grating amplitude and model parameters. We fit both diffraction orders simultaneously. To evaluate the quality of the fit, we use chi-squared

$$\chi^2(x,y) = \sum_{o=1}^{2} \sum_{i=0}^{n} \frac{\left(I^{\mathrm{exp}}_{o,i} - I^{\mathrm{th}}_{o,i}\right)^2}{I^{\mathrm{th}}_{o,i}}, \qquad (4)$$

where $o = 1,2$ are the two diffraction orders and $n = 125$ is the number of voltage values for which the data were acquired. We estimate the parameters by fitting the acquired experimental curves $I^{\mathrm{exp}}(a,x,y)$ for each 20×20 section of the SLM screen (examples are shown in figure 3(b)). We search for the optimal set in the following intervals: $r \in [0,0.15]$ in steps of 0.005, $w \in [0,2]$ pixels in steps of 0.05, $\alpha \in [0,2\pi]$ in steps of 0.1, and $a_{2\pi} \in [190,220]$ in steps of 1. The following two-step optimisation process is used. The goal of the first step is to find the optimal pair (r,w). To this end, we first choose 20 spatial points (x_p,y_p) along the central horizontal cross-section of the raster. We then apply the grid search for each point to find $\alpha(x_p,y_p)$ and $a_{2\pi}(x_p,y_p)$ which minimize $\chi^2(x_p,y_p)$ for each (r,w). We then find, via grid search, the pair of r and w which gives the lowest average $\langle \chi^2(x_p,y_p) \rangle_{x_p,y_p}$. In the subsequent second step, we fit $\alpha(x,y)$ and $a_{2\pi}(x,y)$ over the entire SLM screen. The overall optimization procedure is computed in about 10 h on a notebook with an Intel i5 quad-core processor.

Fitting both orders together significantly improves the accuracy of the parameter estimation. For our SLM, the results were as follows: coverglass reflection coefficient $r = 0.055$, crosstalk Gaussian point spread function width $w = 0.75$ pixels, and the 2π voltage map dropping from 206 in the central part of the SLM to around 197 towards the borders.

Figure 4(a) reports $\alpha(x,y)$ resulting from the fit. As seen, $\alpha(x,y)$ resembles an elliptical paraboloid, with a peak-to-valley value of about 12 rad (1.9λ). To verify the accuracy of the reconstructed $\alpha(x,y)$, we measure it using a commercial wavefront sensor camera (Phasics SID4). To eliminate the

contributions of other optical elements, we also acquire a reference wavefront measurement for a setting in which the SLM is replaced by a flat mirror. Figure 4(b) shows the difference between the phase profiles produced by the two measurements. This difference is consistent with the phase map reconstructed by our method, as evidenced further by comparing one of its cross-sections (figure 4(c)).

In figure 5 we compare the accuracy of our model with three simpler models, in which the crosstalk and/or cavity effects are neglected, i.e. w and/or r are set to zero. The model neglecting both spurious effects (blue curve) is the least accurate (χ^2 is the highest). The quality of the fit improves if the model includes either cavity (orange curve) or crosstalk (purple curve), and is maximum if both effects are taken into account (green curve).

5. Compensation of the spurious effects

We now address the question of how the above characterized spurious effects can be taken into account when using the SLM to produce arbitrary optical fields of amplitude $A(x,y)$ and phase $\Phi(x,y)$. We base our approach on the widely used encoding proposed by Bolduc *et al* [13], in which the pattern printed on the SLM is a modulated blazed grating of the form

$$\theta(x,y) = M(x,y) \cdot \mathrm{mod}\left(F(x,y) + \frac{2\pi x}{\Lambda}, 2\pi\right), \qquad (5)$$

where $M(x,y) \in [0,1]$ and $F(x,y) \in [0,2\pi]$ are slowly varying functions on the scale of the grating period Λ. Similarly to our experimental scheme, the field $E(x,y)$ is subjected to a direct and then inverse Fourier transform by means of two lenses. In the Fourier plane, spatial filtering is implemented to select the first diffraction order. The goal is to choose the functions $M(x,y)$ and $F(x,y)$ such that the field obtained in the image plane is the desired $A(x,y)e^{i\Phi(x,y)}$.

For an ideal SLM modelled in reference [13], the transverse profile of the field after reflection from the SLM surface is given by $E(x,y) = E_0 e^{i\theta(x,y)}$, where E_0 is the incident field. In this case, the amplitude of $E(x,y)$ is constant, but the phase is modulated with the period Λ, with the modulation depth and offset determined by the slowly varying $M(x,y)$ and $F(x,y)$. In an SLM with a cavity effect, however, $E(x,y)$ is given by equation (1), so small amplitude modulation is also present. Importantly, the function $\alpha(x,y)$ is also slowly varying, so the reflected amplitude can still be considered quasiperiodic.

A function of this kind can be expanded into the Fourier series

$$E(x,y) = \sum_{k=-\infty}^{\infty} E^{(k)}_{M,F,\alpha}(x,y) e^{i2\pi kx/\Lambda}, \qquad (6)$$

where the components

$$E^{(k)}_{M,F,\alpha}(x,y) = \frac{1}{\Lambda} \int_{x-\Lambda/2}^{x+\Lambda/2} E(x',y) e^{-i2\pi kx'/\Lambda} dx' \qquad (7)$$

are slowly varying functions of the transverse position. After the spatial filtering of the first diffraction order (i.e selecting
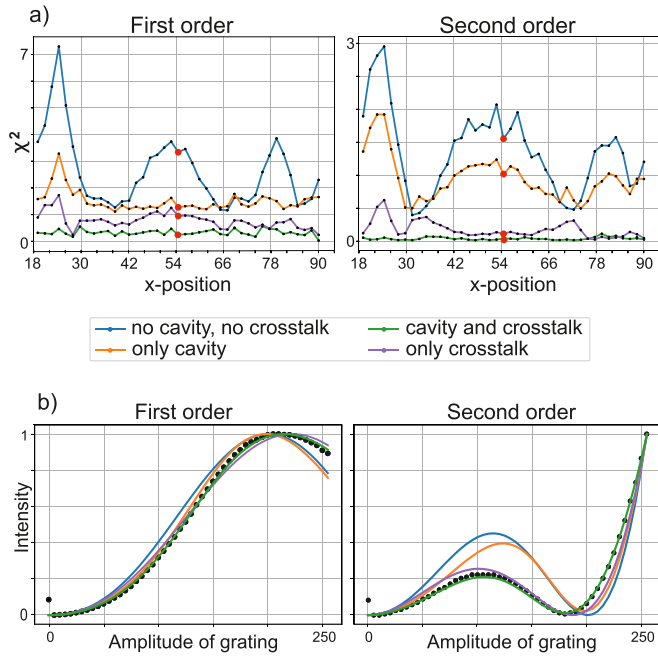
Figure 5. Comparison of the fit quality for the different estimation models. (a) Fit quality parameter $\chi^2(I^{\text{th}}, I^{\text{exp}})$ calculated along an SLM cross-section. (b) Measured (black dot) and fitted (coloured line) intensity response curves for an arbitrary SLM screen position (red dot in (a)).

Figure 6. Algorithm used to calculate an SLM pattern compensating for crosstalk.

$k = 1$), the field in the image plane of the SLM is given by $E_{M,F,\alpha}^{(1)}(x,y)$. We wish this field to match the desired profile:

$$E_{M,F,\alpha}^{(1)}(x,y) = A(x,y)\mathrm{e}^{\mathrm{i}\Phi(x,y)} \tag{8}$$

equation (8) can be numerically solved to obtain $M(x,y)$ and $F(x,y)$ for the given $A(x,y)$ and $\Phi(x,y)$, and thereby construct the cavity corrected hologram. To that end, for each point (x,y) we set up a grid of values $(M(x,y), F(x,y))$, for each of which we evaluate $E(x,y)$ according to equation (1) using $\alpha(x,y)$ and r known from the fit. Subsequently we apply the integral (7) to evaluate $E_{M,F,\alpha}^{(1)}(x,y)$ for each point on the grid, assuming $M(x,y)$ and $F(x,y)$ to be constant within the integration limits. In this way, we obtain a look-up table that allows us to find the pair $(M(x,y), F(x,y))$ for any desired complex output (8) at each point. Note that at this stage it is convenient to neglect the crosstalk, simplifying equation (2) to $\varphi(x,y) = \theta(x,y) + \alpha(x,y)$. More details about this procedure can be found in our Python implementation [30].

To compensate for the crosstalk effect, we modify the hologram $\theta(x,y)$ applying the iterative algorithm shown on figure 6, where $g(x,y)$ is the fitted crosstalk Gaussian kernel. The iterations have to be stopped when the new hologram values are about to exceed the available range of phase modulation. Compared to other crosstalk compensation methods, this approach is not restricted to a specific type of holograms [21], does not reduce the spatial resolution [31] or involve complicated modelling [32].

We evaluate the proposed compensation encoding by generating high-order Hermite-Gaussian (HG) modes. As a figure
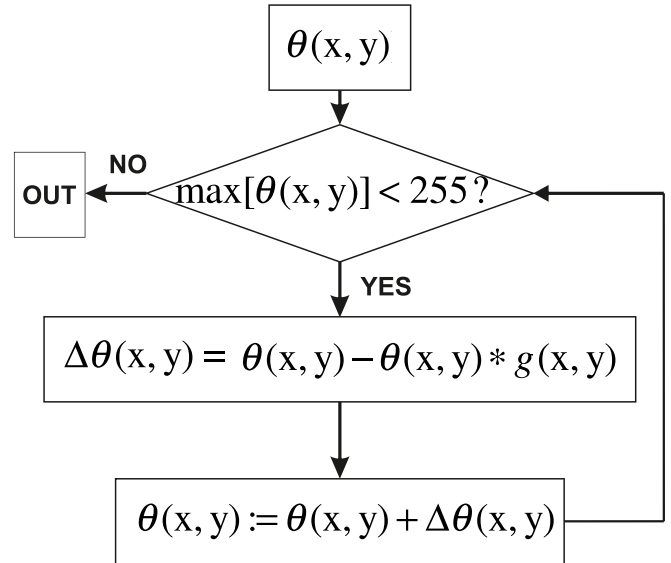
of merit, we evaluate the fidelity of the produced mode with respect to the ideal. For this purpose, we acquire with a camera the near and far field intensity images and apply an iterative maximum-likelihood reconstruction method [33] to obtain the first-order normalized coherence profile

$$g^{(1)}(x,y,x',y') = \frac{\langle E(x,y)E^*(x',y') \rangle}{\int \langle E(x,y)E^*(x,y) \rangle \mathrm{d}x\mathrm{d}y}. \tag{9}$$

The fidelity of the experimental mode is then calculated as

$$F = \int E_{\text{th}}^*(x,y)E_{\text{th}}(x',y')g^{(1)}(x,y,x',y')\mathrm{d}x\mathrm{d}y\mathrm{d}x'\mathrm{d}y',$$

where $E_{\text{th}}(x,y)$ is the normalised theoretical profile of the ideal mode.

An example for $HG_{12,12}$ is shown in figure 7, comparing the theoretical mode profile with those generated by non-, partially- and fully-corrected holograms. The non-compensated hologram (a) produces a mode whose intensity profile has a ring-shaped modulation in the near field (especially visible in the marginal plot below the 3D photograph), due to the Fabry–Perot cavity effect, and distorted in the far field, as a consequence of the curved back panel. The fidelity of this mode with the ideal one is 89.3%. The curvature-corrected hologram (b) generates a mode with a higher fidelity, 92.6%. The far field profile is no longer distorted, but the near field intensity distribution is still modulated by the cavity interference fringes. Hologram (c) compensates both the curvature and cavity effects, producing a mode which best approximates the ideal mode profile (e), with a fidelity of 94.5.

To correct for the crosstalk, we apply the iterations according to figure 6 to the previously calculated curvature- and cavity-compensated hologram. While the fidelity of the produced mode is unchanged, the diffraction efficiency increases by 28%, as seen in figure 7(d). The crosstalk compensation primarily modifies the areas of discontinuity in the phase
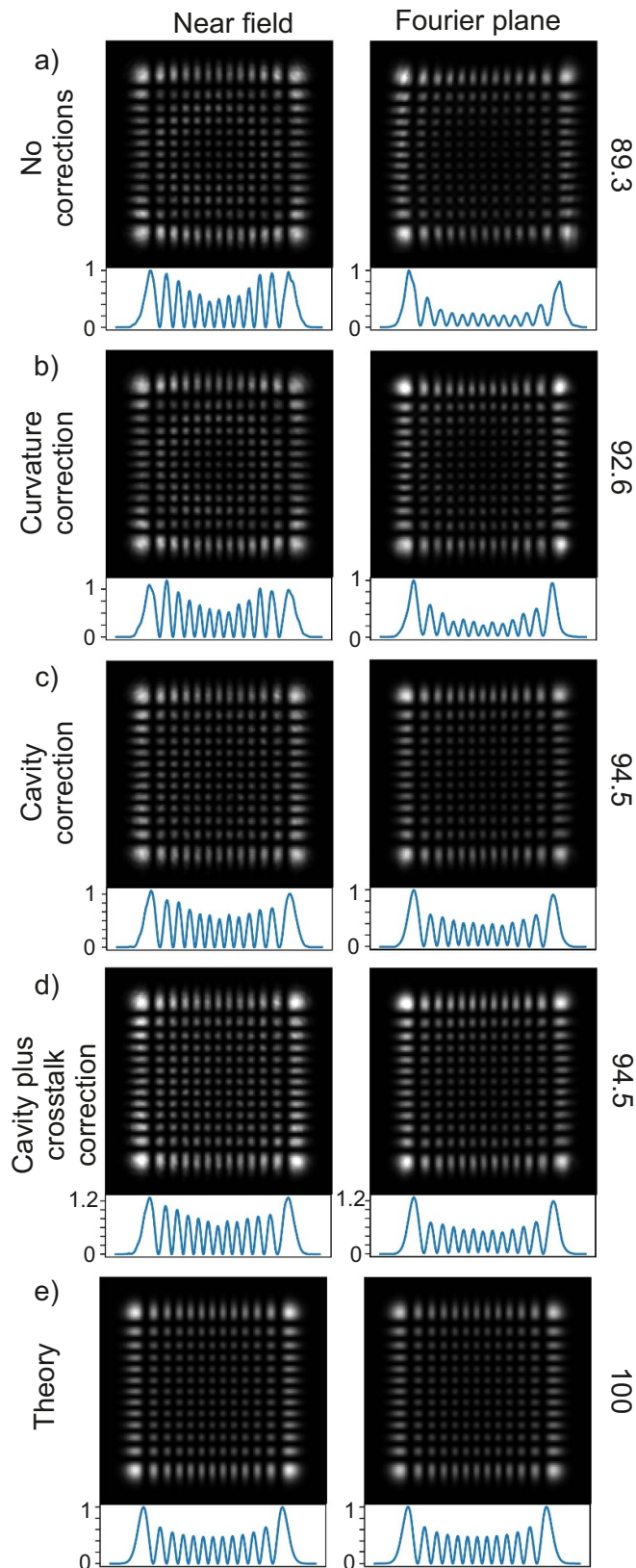
Figure 7. Near- (left) and far-field profiles of the HG$_{12,12}$ as produced by the SLM and measured by a camera (a)–(d) and expected theoretically (e). Each panel indicates the type of correction applied to the SLM hologram and the evaluated fidelity. For each image, the horizontal cross-sections through the mode centre is shown in blue line.

profile $\theta(x, y)$ leading to a sharper blazed grating, whereas the smooth modulation functions $M(x, y)$ and $F(x, y)$ are not affected, which explains the improvement.

6. Conclusion

We optimize the performance of a LCoS SLM by accounting for all its major spurious effects: the curvature of the back panel, the pixel crosstalk and the low-finesse internal cavity. The model parameters are evaluated by measuring the intensity images of the first and second diffraction orders versus the SLM blazed grating amplitude.

Our technique of measuring the back panel curvature is reliant on the Fabry–Perot interference between the front cover glass and the back panel. As such, it is robust to possible curvature of the wave front incident onto the SLM or any other alignment imperfections. In this sense, it is complementary to reference [22] which permits one to study the cumulative spatially-dependent phase shift caused by all optical elements including the SLM.

The presented model, characterization and compensation method can be readily applied to any phase-only LCoS SLM, with potential benefits for a vast range of applications, such as free space mode division multiplexing [34, 35] and maskless interference lithography [36, 37]. Moreover, the ability to generate and manipulate high-order, high-fidelity Hermite-Gaussian modes may have an important impact in super-resolution imaging, paving the way towards the experimental demonstration of Hermite-Gaussian microscopy [38] and related super-resolution techniques based on mode-sorting [39].

Appendix A. Fidelity sensitivity to the spurious effects

To show the sensitivity of the proposed method to the three spurious effects, we performed additional numerical simulations.

To analyse the cavity plus curvature correction, we model an SLM that has a glass-air interface reflection coefficient r that varies from 0 to 0.15, and the backplane curvature that is similar to our SLM (figure 4), but multiplied by a factor within the interval $[0, 2.0]$.

In figure A1(a), we calculate the fidelity of HG$_{12,12}$ without any compensation, i.e. we use the algorithm of reference [13] to compute the SLM hologram directly. The fidelity decreases as the SLM curvature and reflection coefficient increase. In figure A1(b), we compensate only for its curvature, neglecting the cavity effect. For $r = 0$ (no cavity), we notice a significant improvement in the calculated fidelity, which however decreases with increasing r as the cavity effect becomes more significant. Finally, in figure A1(c), we use an SLM hologram that accounts for both the curvature and cavity effect. We see that our algorithm is capable of generating a mode with high fidelity, even when these two effects are significant.
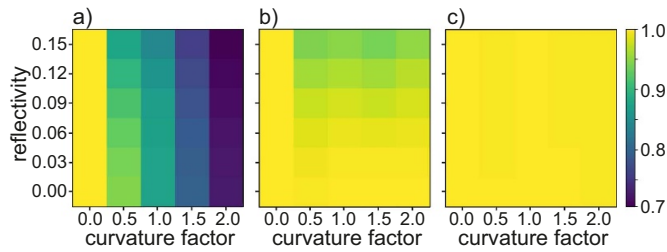
Figure A1. Simulated HG$_{12,12}$ fidelity as a function of the reflection coefficient r and curvature multiplying factor, for (a) uncorrected, (b) curvature corrected and (c) cavity corrected holograms.
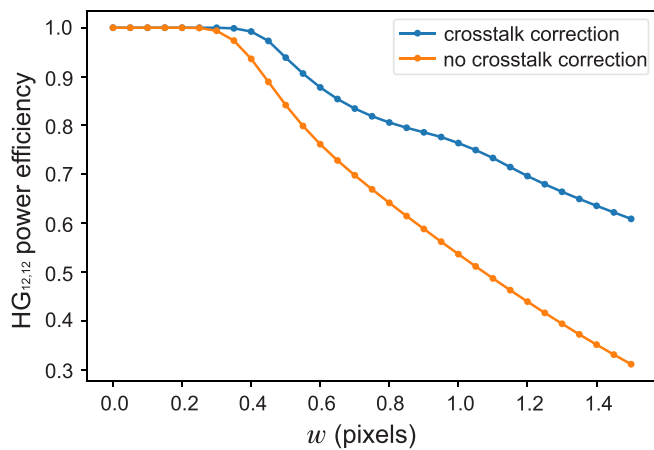

Figure A2. Simulated power efficiency as a function of crosstalk point spread function width with and without the correction.

To characterize the crosstalk correction, we model the diffraction efficiency of the mode produced by the hologram corrected for the crosstalk effect and compare it with a hologram with no corrections. We plot the efficiency versus the width of the crosstalk point spread function in figure A2. As seen, the crosstalk correction significantly improves the efficiency for high widths. Both the reflectivity of the air-glass interface and curvature of the back panel are set to zero for this simulation. As mentioned previously, the influence of the crosstalk on the fidelity is insignificant.

ORCID iD

A A Pushkina https://orcid.org/0000-0002-1273-4787

References

[1] Sit A *et al* 2017 High-dimensional intracity quantum cryptography with structured photons *Optica* **4** 1006–10
[2] Parigi V, D'Ambrosio V, Arnold C, Marrucci L, Sciarrino F and Laurat J 2015 Storage and retrieval of vector beams of light in a multiple-degree-of-freedom quantum memory *Nat. Commun.* **6** 7706
[3] Angelo J P, Van de Giessen M and Gioux S 2017 Real-time endoscopic optical properties imaging *Biomed. Opt. Express* **8** 5113–26
[4] McClatchy D M, Rizzo E J, Wells W A, Cheney P P, Hwang J C, Paulsen K D, Pogue B W and Kanick S C 2016 Wide-field quantitative imaging of tissue microstructure using sub-diffuse spatial frequency domain imaging *Optica* **3** 613–21
[5] Ng J, Lin Z and Chan C 2010 Theory of optical trapping by an optical vortex beam *Phys. Rev. Lett.* **104** 103601
[6] Arlt J, Garcés-Chávez V, Sibbett W and Dholakia K 2001 Optical micromanipulation using a Bessel light beam *Opt. Commun.* **197** 239–45
[7] Ren Z and Lam E Y 2016 Super-resolution imaging in optical scanning holography using structured illumination *Proc. SPIE* **10022** 1002203
[8] Larocque H, Sugic D, Mortimer D, Taylor A J, Fickler R, Boyd R W, Dennis M R and Karimi E 2018 Reconstructing the topology of optical polarization knots *Nat. Phys.* **14** 1079
[9] Hermosa N, Rosales-Guzmán C, Pereira S and Torres J 2014 Nanostep height measurement via spatial mode projection *Opt. Lett.* **39** 299–302
[10] Reicherter M, Haist T, Wagemann E and Tiziani H J 1999 Optical particle trapping with computer-generated holograms written on a liquid-crystal display *Opt. Lett.* **24** 608–10
[11] Yan Y, Yue Y, Huang H, Ren Y, Ahmed N, Tur M, Dolinar S and Willner A 2013 Multicasting in a spatial division multiplexing system based on optical orbital angular momentum *Opt. Lett.* **38** 3930–3
[12] Osten W, Kohler C and Liesener J 2005 Evaluation and application of spatial light modulators for optical metrology *Opt. Pura Apl.* **38** 71–81
[13] Bolduc E, Bent N, Santamato E, Karimi E and Boyd R W 2013 Exact solution to simultaneous intensity and phase encryption with a single phase-only hologram *Opt. Lett.* **38** 3546–9
[14] Zhu L and Wang J 2014 Arbitrary manipulation of spatial amplitude and phase using phase-only spatial light modulators *Sci. Rep.* **4** 7441
[15] Zhang Z, You Z and Chu D 2014 Fundamentals of phase-only liquid crystal on silicon (LCOS) devices *Light: Sci. Appl.* **3** E213
[16] Harriman J L, Linnenberger A and Serati S A 2004 Improving spatial light modulator performance through phase compensation *Proc. SPIE* **5553** 58–67
[17] Xun X and Cohn R W 2004 Phase calibration of spatially nonuniform spatial light modulators *Appl. Opt.* **43** 6400–6
[18] Kulick J H, Jarem J M, Lindquist R G, Kowel S T, Friends M W and Leslie T M 1995 Electrostatic and diffraction analysis of a liquid-crystal device utilizing fringing fields: applications to three-dimensional displays *Appl. Opt.* **34** 1901–22
[19] Apter B, Efron U and Bahat-Treidel E 2004 On the fringing-field effect in liquid-crystal beam-steering devices *Appl. Opt.* **43** 11–19
[20] Gemayel P, Colicchio B, Dieterlen A and Ambs P 2016 Cross-talk compensation of a spatial light modulator for iterative phase retrieval applications *Appl. Opt.* **55** 802–10
[21] Persson M, Engström D and Goksör M 2012 Reducing the effect of pixel crosstalk in phase only spatial light modulators *Opt. Express* **20** 22334–43
[22] Cizmár T, Mazilu M and Dholakia K 2010 In situ wavefront correction and its application to micromanipulation *Nat. Photon.* **4** 388
[23] Zhang Z, Yang H, Robertson B, Redmond M, Pivnenko M, Collings N, Crossland W A and Chu D 2012 Diffraction based phase compensation method for phase-only liquid crystal on silicon devices in operation *Appl. Opt.* **51** 3837–46
[24] Martínez J L, Moreno I, del Mar Sánchez-López M, Vargas A and García-Martínez P 2014 Analysis of multiple internal

reflections in a parallel aligned liquid crystal on silicon SLM *Opt. Express* **22** 25866–79

[25] Bowman D *et al* 2017 High-fidelity phase and amplitude control of phase-only computer generated holograms using conjugate gradient minimisation *Opt. Express* **25** 11692–700

[26] Jesacher A, Schwaighofer A, Fürhapter S, Maurer C, Bernet S and Ritsch-Marte M 2007 Wavefront correction of spatial light modulators using an optical vortex image *Opt. Express* **15** 5801–8

[27] Davis J A, Cottrell D M, Campos J, Yzuel M J and Moreno I 1999 Encoding amplitude information onto phase-only filters *Appl. Opt.* **38** 5004–13

[28] Lazarev G, Chen P J, Strauss J, Fontaine N and Forbes A 2019 Beyond the display: Phase-only liquid crystal on Silicon devices and their applications in photonics *Opt. Express* **27** 16206–49

[29] Hällstig E, Stigwall J, Martin T, Sjöqvist L and Lindgren M 2004 Fringing fields in a liquid crystal spatial light modulator for beam steering *J. Mod. Opt.* **51** 1233–47

[30] Pushkina A, Costa-Filho J, Maltese G and Lvovsky A 2020 Python program to generate phase-only SLM holograms (https://github.com/giomalt/SLM_hologram_generation)

[31] Carbonell-Leal M and Mendoza-Yero O 2019 Encoding complex fields by using a phase-only optical element: mitigation of pixel crosstalk effects arXiv:1903.06046

[32] Moser S, Ritsch-Marte M and Thalhammer G 2019 Model-based compensation of pixel crosstalk in liquid crystal spatial light modulators *Opt. Express* **27** 25046–63

[33] Lvovsky A 2004 Iterative maximum-likelihood reconstruction in quantum homodyne tomography *J. Opt. B: Quantum Semiclass. Opt.* **6** S556

[34] Forbes A, Dudley A and McLaren M 2016 Creation and detection of optical modes with spatial light modulators *Adv. Opt. Photon.* **8** 200–27

[35] Wang J *et al* 2012 Terabit free-space data transmission employing orbital angular momentum multiplexing *Nat. Photon.* **6** 488

[36] Behera S and Joseph J 2017 Design and realization of functional metamaterial basis structures through optical phase manipulation based interference lithography *J. Opt.* **19** 105103

[37] Xavier J and Joseph J 2011 Tunable complex photonic chiral lattices by reconfigurable optical phase engineering *Opt. Lett.* **36** 403–5

[38] Yang F, Tashchilina A, Moiseev E S, Simon C and Lvovsky A I 2016 Far-field linear optical superresolution via heterodyne detection in a higher-order local oscillator mode *Optica* **3** 1148–52

[39] Tsang M, Nair R and Lu X M 2016 Quantum theory of superresolution for two incoherent optical point sources *Phys. Rev.* X **6** 031033